J Geophys (1986) 60:149–156

Journal of Geophysics

# Lateral variations of the structure of the crust-mantle boundary from conversions of teleseismic *P* waves

**Liu Qiyuan** [1] **and Rainer Kind** [2]

[1] Institute of Geology, State Seismological Bureau, P.O. Box 634, Beijing, China
[2] Seismologisches Zentralobservatorium Gräfenberg, Krankenhausstraße 1, 8520 Erlangen, Federal Republic of Germany

**Abstract.** Clear *P*-to-*S* converted phases are observed in teleseismic seismograms recorded at the Gräfenberg array. The seismic events used are nuclear explosions from east Kasakh and deep-focus earthquakes from the region of Japan and central Asia. The identification of the converted phases has been improved by the rotation of the coordinate system. Theoretical seismograms have been computed to obtain the response of various velocity structures of the lithosphere under the receivers, using the reflectivity method of Kind (1985) for different source and receiver structures. The interpretation of the *P*-to-*S* conversions leads to a model of the crust-mantle transition zone with a first-order discontinuity and a normal velocity contrast in the north, an increased velocity contrast in the centre, and a reduced sharpness of the discontinuity in the south of the array. The sedimentary layers underneath the stations also cause strong converted phases, and they also influence strongly the waveform of the incoming *P* wave.

**Key words:** Lateral inhomogeneities – *P*-to-*S* conversions – Theoretical seismograms

## Introduction

In recent years conversions of teleseismic body waves have been extensively used for exploring the structure of the earth (Bath and Stefansson, 1966; Polshkov et al., 1973; Vinnik, 1977; Vinnik et al., 1983; Burdick and Langston, 1977; Langston, 1979; Faber and Müller, 1980, 1984; Bock and Ha, 1984). Extensive experiments have been carried out in China, where *P*-to-*S* converted waves in the *P*-wave group of strong deep-focus events have been observed along profiles of about 3,000 km length (Shao et al., 1978, 1985). The results have been used for investigations of the common features of the deep structures in areas of strong earthquakes (Shao et al., 1985).

It has been shown that the converted phases can be used not only for determining the depth of discontinuities in the earth, but also for investigating their lateral fluctuations. This can be done because a specific converted phase within the body wave train is associated with a specific interface and its time delay and energy depends mainly on the depth and structure of the interface underneath the receiver.

*Offprint requests to:* R. Kind

The development of digital event recorders, particularly of digital broad-band arrays, will contribute to a more reliable and more convenient identification of converted phases because these new systems provide high-quality records and simplify data processing. In addition, the computation of theoretical seismograms is a powerful tool for the interpretation of seismic phases. The information about the fine structure of the lithosphere can be obtained from the broad-band or short-period seismograms.

Our purpose is to investigate the lateral inhomogeneities of the lithosphere under the Gräfenberg array (GRF) by using converted and multiply reflected waves which have been recorded by the three-component stations of the array. Our method is different from the method of Aki et al. (1976) or the method used by Faber et al. (1986) to determine the three-dimensional structure under arrays, which used *P*-wave travel-time delays. The observations of converted phases provide information about existence, location and sharpness of discontinuities and not about averaged velocities in block structures.

## Method

The method is based on the identification of converted or multiply reflected phases within the first 10 s of the direct *P* wave. These phases are used to determine the interface depth and the velocity distribution within the lithosphere under a station. Lateral inhomogeneities of the lithosphere may then be derived by comparing these results at each station. It has been shown by observational and theoretical studies that, in China, there are several *PS* converted phases within the first 10 s of the direct teleseismic *P* wave train which can be identified on the rotated *SV* component of short-period records (Shao et al., 1978; Liu and Shao, 1985). The common features of the *PS* converted phases are described in these papers:

1) The time delays of phases converted at shallow structures depend mainly on the receiver structure and their variations are quite small with the epicentral distances.

2) The energy of *PS* conversions bears a close relation to the interface structure where the incoming wave is converted. *PS* conversions strong enough to be identified can be generated not only on sharp discontinuities, but also at other structures like gradients or stacks of thin layers.

3) The *PS* waveforms are generally quite similar to the ones of the original direct *P* wave, even if they are generated at stacks of thin layers.

**Table 1.** List of the events used (after PDE). $AZ$ denotes back azimuth and $i_o$ denotes the experimentally determined best angle of incidence

| No. | Date | Origin time | Latitude | Longitude | Depth (km) | $m_b$ | Distance | $AZ$ degrees | $i_o$ |
|---|---|---|---|---|---|---|---|---|---|
| 15 | 831008 | 07 45 26.6 | 44.2N | 130.7E | 558 | 5.7 | 72.6 | 41 | 1 |
| 14 | 840420 | 06 31 10.6 | 50.1N | 148.7E | 582 | 6.0 | 74.1 | 27 | 1 |
| 13 | 840415 | 07 34 12.0 | 42.9N | 131.1E | 538 | 5.0 | 73.8 | 42 | 1 |
| 12 | 810531 | 23 59 35.2 | 44.6N | 137.3E | 295 | 5.4 | 75.0 | 37 | 1 |
| 11 | 820714 | 10 42 13.5 | 45.6N | 143.4E | 325 | 5.3 | 76.3 | 32 | 1 |
| 10 | 830928 | 08 04 47.6 | 41.2N | 132.5E | 513 | 5.1 | 75.9 | 42 | 1 |
| 9 | 830928 | 07 59 13.9 | 41.2N | 132.5E | 522 | 5.1 | 75.9 | 42 | 1 |
| 8 | 830912 | 15 42 08.5 | 36.5N | 71.1E | 209 | 6.1 | 44.5 | 84 | 2 |
| 7 | 841027 | 01 50 10.6 | 50.0N | 78.8E | 0 | 6.2 | 44.7 | 69 | 4 |
| 6 | 840714 | 01 09 10.5 | 49.9N | 79.0E | 0 | 6.2 | 42.3 | 63 | 4 |
| 5 | 840526 | 03 13 12.4 | 50.0N | 79.1E | 0 | 6.0 | 42.4 | 62 | 4 |
| 4 | 840425 | 01 09 03.5 | 50.0N | 78.9E | 0 | 5.9 | 42.3 | 63 | 4 |
| 3 | 840329 | 05 19 08.2 | 49.9N | 79.0E | 0 | 5.9 | 42.4 | 63 | 4 |
| 2 | 840219 | 03 57 03.4 | 49.9N | 78.8E | 0 | 5.8 | 42.3 | 63 | 4 |
| 1 | 820704 | 01 17 14.4 | 50.0N | 78.9E | 0 | 6.1 | 42.2 | 63 | 4 |

4) A sedimentary layer with low velocity and high absorption is able to enhance the energy of $PS$ conversions on the radial component.

A data processing procedure has been used in this paper to improve the identification of the $PS$ conversions and the multiple reflections. The first step is to rotate the coordinate system in order to search for $PS$ conversions (Vinnik 1977; Langston 1979). We denote

$$P(t) = Z(t)*\cos(i_o) + R(t)*\sin(i_o)$$
$$Q(t) = -R(t)*\cos(i_o) + Z(t)*\sin(i_o)$$
$$R(t) = X(t)*\cos(AZ) + Y(t)*\sin(AZ)$$
$$T(t) = Y(t)*\cos(AZ) - X(t)*\sin(AZ)$$

where $Z(t)$, $X(t)$ and $Y(t)$ are the vertical, north and east components of a seismogram, respectively. $AZ$ is the back azimuth; $i_o$ is the angle of incidence. In a laterally homogeneous and isotropic earth, $SH$ waves should be recorded only on the $T$ component. $P$ and $SV$ waves are recorded on the $Z$ and $R$ components, but the $Q$ component should only have $SV$ waves and the $P$ component should only have $P$ waves, provided the correct angle of incidence is chosen.

However, the uppermost part of the lithosphere is often laterally very inhomogeneous, therefore the separation of an incoming wave in its various wave types is not always easy. Experiments with varied back azimuths and angles of incidence must therefore be carried out in order to find the best signal enhancement of the converted phases. The first converted wave after the direct $P$ wave often has such a short time delay that it interferes with the projection of the direct $P$ wave on the horizontal components. Therefore, the choice of the proper angle of incidence is in this case especially critical. Plesinger et al. (1986) describe a method for the determination of azimuth and angle of incidence of incoming waves. This method has been used to determine the angle of incidence in this paper.

Another important step in the analysis method is the selection of events with simple source functions. Such events are very often deep-focus events. Nuclear explosions also have simple source functions. Therefore, we have restricted our data base to these two types of events.

The summation of the same components of events with the same epicentral distance increases the signal-to-noise ratio. This procedure greatly improves the reliability of the phase identification.

If converted phases are identified in the data, then a starting model of the structure under the station can be derived for the computation of theoretical seismograms. When the epicentral distance is greater than 40°, the depth $h$ of the interface can be determined approximately by:

$$h = (V_p*\Delta T_{ps})/(K-1)$$
$$K = V_p/V_s$$

where $V_p$ and $V_s$ are the average $P$ and $S$ velocities, respectively, and $\Delta T_{ps}$ is the time delay of the $PS$ wave relative to the direct $P$ wave.

It has been shown that multiple reflections should be considered when theoretical seismograms of conversions are computed (Liu and Fan, 1985). Therefore, the new version of the reflectivity method by Kind (1985) has been used for calculating theoretical seismograms in order to infer the velocity distributions. This method can be used for different source and receiver structures and the multiple waves are automatically taken into account.

## Data

The GRF array has been described in detail by Harjes and Seidl (1978). The 15 events used here are listed in Table 1. The seismograms recorded by the three-component GRF stations A1, B1, C1 are given in Figs. 1–3, respectively. A1 is located in the north, B1 in the centre, and C1 in the south of the array. Figures 1–3 show the seismograms after the rotations mentioned above. The back azimuths and the observed angles of incidence are also listed in Table 1. The angles of incidence in Table 1 are too small for the epicentral distances of the events. If horizontal layering is assumed, then only unrealistic low velocities of the sediments could explain these small angles. In order to show the correctness of these observations we show particle-motion diagrams of the stations A1, B1 and C1 in Fig. 4 for event 1 in Table 1. This figure shows clearly that the angle of incidence at the GRF stations is extremly small. For comparison, particle motions of the stations KHC (Kasperske Hory, Chechoslovakia) and KSP (Ksiaz, Poland) are also shown in Fig. 4. These two stations have more normal angles of incidence.

The reason for this anomaly at the GRF stations is

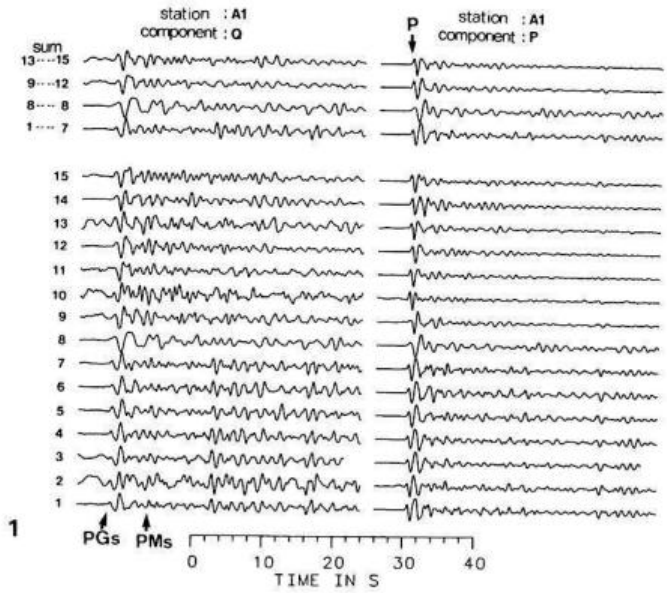


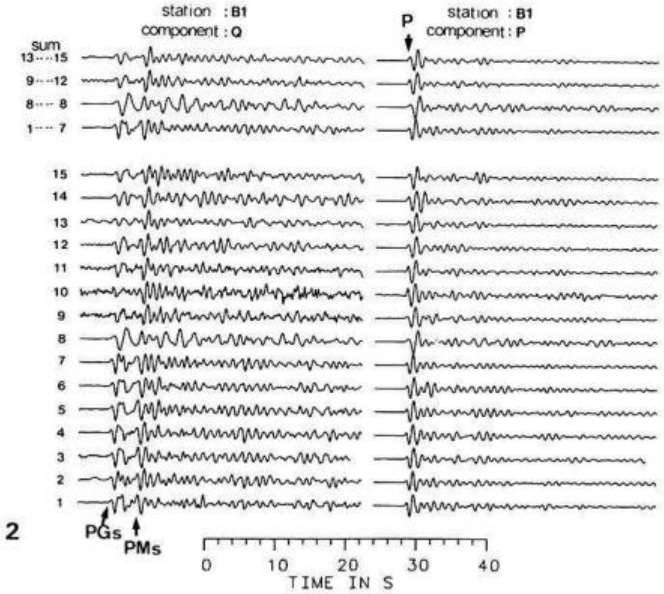


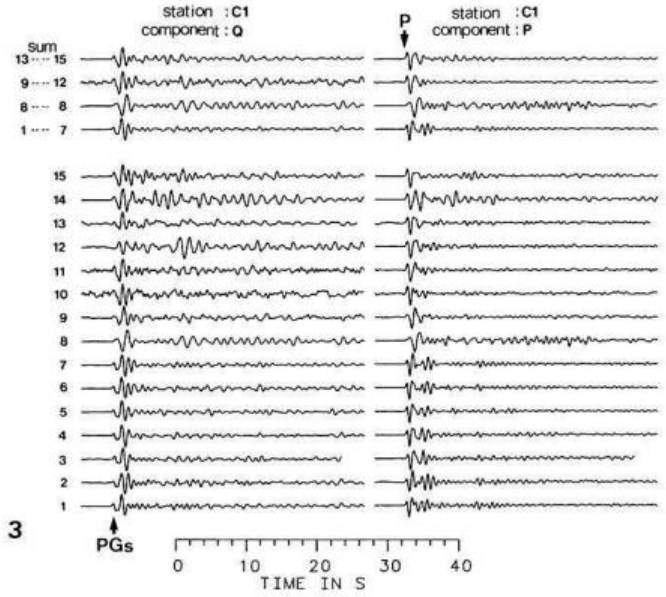


**Fig. 1.** Rotated $Q$ and $P$ components of WWSSN short-period simulations of events recorded at station A1. The numbers 1–15 refer to the event numbers in Table 1. Summation traces of groups of events are plotted at the *top of the figure*. The labelled phases are: *PMs*-converted *S* wave at the Moho, *PGs*-converted *S* wave at the bottom of the sediments, *P*-incoming *P* wave. All traces are independently normalized to the same size. The *PMs* conversion is much smaller than the *PGs* conversion. See Figs. 6 and 7 for a comparison of the amplitudes of the different traces

**Fig. 2.** Same as in Fig. 1, for station B1. The Moho conversion *PMs* is much stronger at station B1 than at A1

**Fig. 3.** Same as in Fig. 1, for station C1. The Moho conversion *PMs* is not visible at all

still unknown. Array slownesses of the same events, determined from *P*-wave arrival times of all vertical components, are not in agreement with such small angles of incidence. This could indicate that the anomaly is located at shallow depth. It should be kept in mind that this observation is made with short-period data. The anomaly underneath GRF makes the comparison with theoretical seismograms more difficult. We can at present only assume that the anomaly only rotates the angle of incidence without too many other complications. Another observation in Fig. 4 is also interesting: the particle motion at KHC and KSP is more linearly polarized than at GRF, where the polarization is more elliptical. This is an indication of the presence of more (delayed) shear waves in the *P*-wave group at GRF, due to conversions at the sediments. In spite of the small angle of incidence at GRF, the rotation into $P$ and $Q$ components has been performed. If the angle of incidence is, for example, 4°, then about 7% of the relatively large vertical component is added to the radial component in order to compute $Q$ (see previous section).

Figures 1–3 show the WWSSN short-period simulations. Figure 5 shows the broad-band seismograms recorded at station B1. It can clearly be seen from broad-band data in Fig. 5 that all of the deep events and explosions used here have quite simple source time functions. The comparison of the WWSSN short-period simulations (Fig. 2) and the broad-band records (Fig. 5) at station B1 shows that all chosen events have mainly short-period energy and that the signal-to-noise ratio is much better for the WWSSN simulations. Therefore, we have used only the WWSSN short-period simulations in the following.

Figures 6 and 7 show the amplitude comparison of the energy on the three rotated components for some events. There is a clear phase shift between the $P$ and the $Q$ components in the first cycles; the $Q$ component is delayed. This indicates that the energy on the $Q$ component is converted shear wave energy, which arrives later and is not a projection from the $P$ wave.

Each trace in Figs. 1–3 and 5 is normalized independently to its maximum amplitude. The correlation of weak

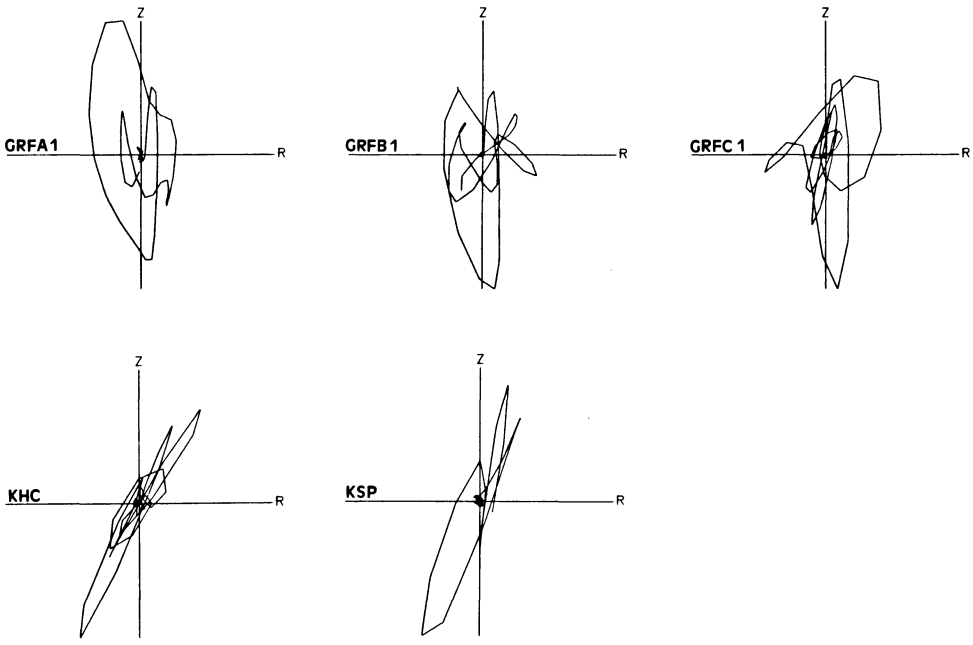


**Fig. 4.** Broad-band particle-motion diagrams of the first 5 s for event 1 in Table 1 at the GRF stations A1, B1 and C1, and at the stations KSP (Poland) and KHC (Chechoslovakia). The angle of incidence is abnormally small under the GRF array

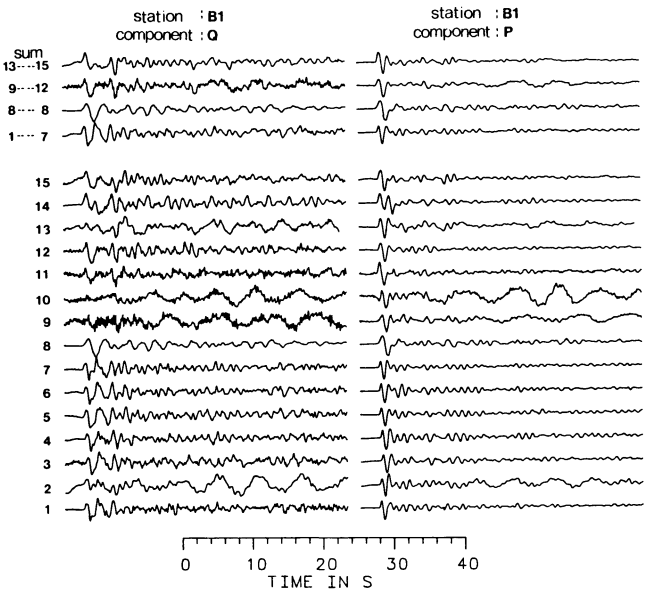


**Fig. 5.** Broad-band records at station B1 of the same data as in Fig. 2. The signal-to-noise ratio of the converted phases is better in the short-period data of Fig. 2 than here

phases, labelled *PGs* and *PMs* and interpreted as conversions at the bottom of the sediments or at the Moho, respectively, is made much clearer this way over a number of different events. But the relative amplitude information is lost in Figs. 1–3. In the *Q* component of Figs. 1 and 3 *PGs* is the strongest phase, and in Fig. 2 it is *PMs*. The amplitudes of these phases can be compared in Figs. 6 and 7 for some events. These figures show that *PGs* and *P* vary strongly across the array. *PGs* is largest at C1 and weakest at B1 and the *P* wave is often smallest at B1. The Moho conversion *PMs* is strongest at B1, weaker at A1 and not visible at C1. These observations indicate that their interpretation could lead to new information about the structure of the Moho underneath the GRF array. Travel-time variations of the converted phases across the array are difficult to observe in our data. Therefore, no Moho depth variations can be derived. Summation traces of groups of events from one region have been computed (see Figs. 1–3 and 5) in an attempt to improve the signal-to-noise ratio. But it seems that more earthquakes from one region are required to obtain a significant improvement.

## Theoretical seismograms

The most recent extension by Kind (1985) of the reflectivity method allows the computation of theoretical seismograms for models which have different structures at the sites of the stations and at the epicentre and a common model of the mantle underneath. The complete response in each of the three parts of the model is computed and only selected wave fields are permitted to penetrate through the boundaries between the different parts of the model. This method is very useful for comparisons with the type of data we are interpreting in this study, since the structure at the source can be kept fixed.

Since our data consist of records of nuclear explosions and deep-focus earthquakes with unknown source orientation, we have used a hypothetical explosive source at a depth of 80 km in our model, which allows a comparison of the theoretical seismograms with both types of data. The large depth was chosen in order to avoid complications due to crustal structure near the source. We think that the differences between the real situation and our model do not influence our results significantly, since we are using averaged observations of many different events. We used an epicentral distance of 50° and simulated the WWSSN short-period response in our theoretical seismograms, which was also simulated in most of the data.

At the beginning we investigated the influence of different structures of the crust-mantle boundary on the shear waves converted at this boundary. In Fig. 8 are shown theoretical seismograms of *Q* and *P* components for a number of different Moho structures. The models belonging to the seismograms in Fig. 8 are given in Table 2. All models in

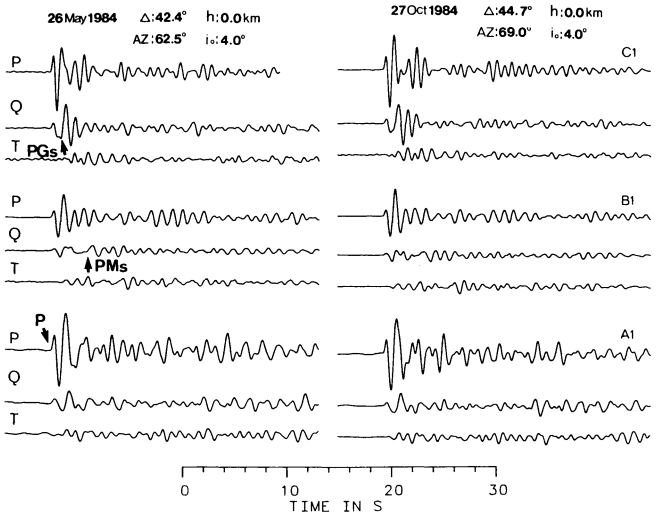


**Fig. 6.** *P*, *Q* and *T* components of the events 5 (*left*) and 7 (*right*). The amplitudes of one event are all on the same scale, so that they can be compared at the different components. There is a clear phase shift between the *P* and *Q* components in the first few cycles, indicating that we have delayed *S* energy on the *Q* component and not projected *P* energy. The transformation angles *AZ* and $i_0$ are experimentally determined by optimizing the energy at the appropriate component

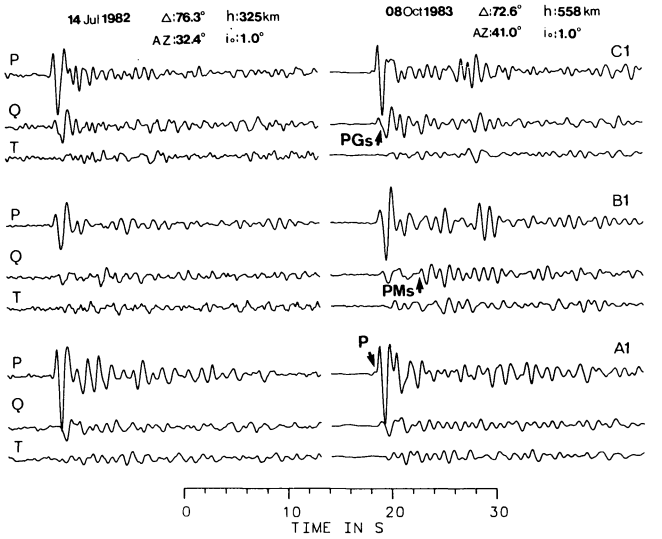


**Fig. 7.** Same as in Fig. 6, for the events 11 (*left*) and 15 (*right*)

Fig. 8 have no surficial sediments; the averaged crustal material extends to the free surface. The angle of incidence was chosen as 25° for the computation of the *Q* and *P* components from the *R* and *Z* components. This is not exactly the true angle of incidence for the model used, but it permits a small portion of the *P* wave to be seen on the *Q* component. The shear waves are not influenced significantly on the *Q* component by this manipulation and the relative position of the *P* waves remains visible.

The angles of incidence of the observed and theoretical data are very different. Since the reason for the unusually small observed angle of incidence is not yet certain, we have not attempted to model this with theoretical seismograms. We have rotated both types of data with their different angles of incidence, in order to obtain the optimum energy of the converted waves on the *Q* component. The amplitude of the *Q* component is enhanced 5 times in Fig. 8 relative to the *P* component. A comparison with Figs. 6 and 7 shows that the observed energy on the *Q* component is much larger relative to the *P* component than the theoretical ratio in Fig. 8. Therefore, the theoretical seismograms in Fig. 8 can be used only for a comparison of the converted waves at different Moho structures.

Trace 1 in Fig. 8 shows, for comparison, results from a model without a crustal layer. Trace 2 is for a first-order discontinuity and has a well-developed *PMs* conversion. Traces 3, 4 and 5 are for gradient zones with increasing thickness, which reduces the conversions gradually in size. The thickness of the transition zone has to be comparable to the wavelength to substantially reduce the conversion. A large reduction of the size of the converted phase is achieved by just one thin high-velocity layer above the Moho (trace 6). Since the main frequencies are near 1 Hz, the dominant wavelength is 8 km in the high-velocity material and 6 km in the crustal material. Several high- and low-velocity lamellas (see traces 7–11) increase the complex-

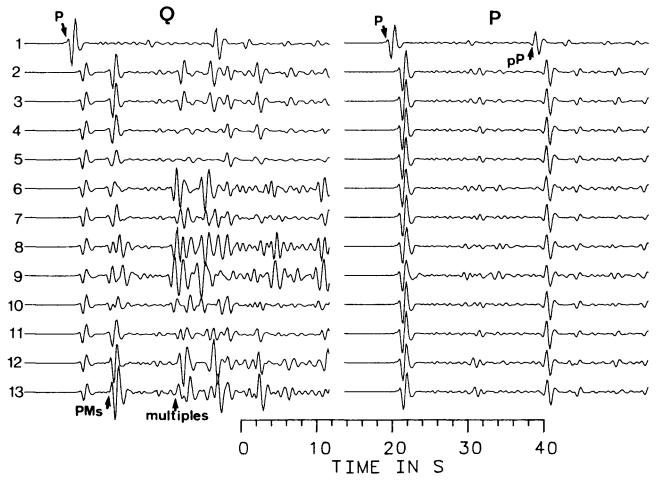


**Fig. 8.** *Q* and *P* components of theoretical seismograms for different Moho structures. *The numbers* refer to the Moho structures in Table 2. The amplitudes of the *Q* component are 5 times enlarged relative to those of the *P* component. All traces are rotated using an angle of incidence of 25°

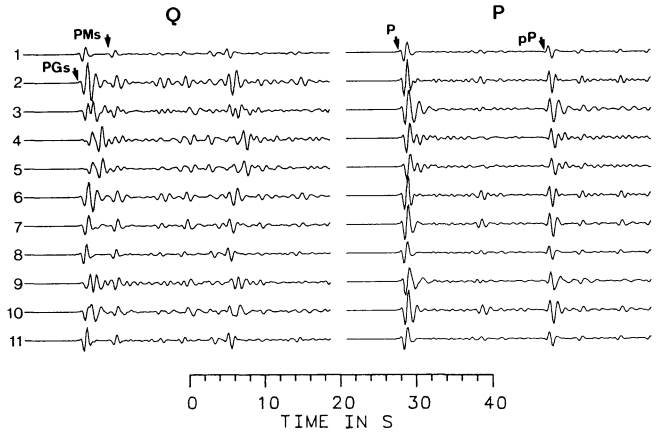


**Fig. 9.** *Q* and *P* components of theoretical seismograms for different structures of the sediments. *The numbers* refer to the sedimentary structures in Table 3. The amplitudes of the *Q* component are 2 times enlarged relative to those of the *P* component. All traces are rotated using an angle of incidence of 10°

**Table 2.** Model parameters of the crust-mantle transition zone used for the computation of theoretical seismograms in Fig. 8. The centre of the transition zone is always placed at 30 km depth. High-velocity lamellas have the velocity of the uppermost mantle (8 km/s); between the high-velocity layers are layers with 6 km/s and the same thickness; the low-velocity zones (Nos. 12 and 13) have a velocity of 5 km/s. *P* velocities are given. *S* velocities are obtained by dividing the *P* velocities by the square root of 3. The densities are obtained from Birch's law (density = 0.252 + 0.3788**P* velocity)

| No. | Parameters of Moho transition zone |
|---|---|
| 1 | No crust, mantle with velocity 8 km/s extends to surface |
| 2 | First-order Moho at 30 km, crustal velocity 6 km/s |
| 3 | 1 km linear gradient |
| 4 | 3 km linear gradient |
| 5 | 6 km linear gradient |
| 6 | 1 high-velocity lamella 1.0 km thick |
| 7 | 2 high-velocity lamellas 0.5 km thick |
| 8 | 2 high-velocity lamellas 1.0 km thick |
| 9 | 2 high-velocity lamellas 1.5 km thick |
| 10 | 4 high-velocity lamellas 0.5 km thick |
| 11 | 4 high-velocity lamellas 0.2 km thick |
| 12 | Low-velocity layer 1 km thick above Moho |
| 13 | Low-velocity layer 2 km thick above Moho |

**Table 3.** Model parameters of sedimentary models used for the computation of theoretical seismograms in Fig. 9. *P* velocities are given, *S* velocities and densities are obtained as in Table 2

| No. | Parameters of the sedimentary models |
|---|---|
| 1 | No sediments, crust with 6 km/s extends to surface |
| 2 | 0.5 km sediments, 3.0 km/s |
| 3 | 1.0 km sediments, 3.0 km/s |
| 4 | 2.0 km sediments, 3.0 km/s |
| 5 | Like model 4, but upper 200 m replaced with 5 km/s |
| 6 | Like model 2, but upper 200 m replaced with 5 km/s |
| 7 | Linear gradient from surface (3 km/s) to 2.0 km depth |
| 8 | Linear gradient from surface (3 km/s) to 0.5 km depth |
| 9 | 1.5 km sediments, 3.5 km/s (models sediments under A1) |
| 10 | 0.9 km sediments, 3.5 km/s (models sediments under B1) |
| 11 | 0.3 km sediments, 3.5 km/s (models sediments under C1) |

ity of the converted wave. A large increase in the size of the converted phase is achieved by a low-velocity layer above the Moho (see traces 12 and 13).

Another observation in the *Q* component of Fig. 8 is that most traces have much energy beginning about 12 s after the *P* onset. This energy is due to incoming shear waves which have been multiply reflected within the crust. Traces 4 and 5 (belonging to 3- and 6-km-thick transition zones at the Moho) and traces 10 and 11 (belonging to transition zones with high-velocity lamellas) have significantly less multiples than all other models of the Moho.

The result from this study of *P*-to-*S* conversions at a number of Moho transition zones in Fig. 8 and Table 2 is that simple model perturbations can significantly alter the size of the converted phase. A thin (relative to the wavelength) high-velocity layer above the Moho, or a thick transition zone, reduces, and a thin low-velocity layer, also above the Moho, increases the size of the converted phase. The models discussed in Fig. 8 are not a complete or a very systematic search through all the possible models. Also, the relation between the frequency content of the incoming signal and the layer thickness could be studied further. But we think that the theoretical seismograms shown in Fig. 8 indicate how the conversions at the Moho can be influenced by modifications of the structure of the crust-mantle boundary. The *P*-wave signal form or amplitude (Fig. 8) is not influenced very much by the different forms of the transition zone between the crust and the mantle.

The other significant structure which could influence the recorded wave fields are the sedimentary layers beneath the stations. Figure 9 shows *Q* and *P* components for a number of sedimentary models. The Moho is assumed to be a first-order discontinuity at 30 km depth, and a homogeneous crust with a velocity of 6 km/s extends up to the sediments. The *Q* and *P* components are computed from the *R* and *Z* components by assuming an angle of incidence of 10°. The different sedimentary models used for the theoretical seismograms in Fig. 9 are described in Table 3. The *P* component in Fig. 9 is multiplied by a factor 0.5 relative to the *Q* component in the same figure.

The presence of the sedimentary layers amplifies the amplitudes of both components, but the *Q* component, i.e. the converted phases, is much more amplified by the sediments beneath a station (trace 1 in Fig. 9 belongs to a model with no sediments for comparison). The conversion at the bottom of the sediments is labelled *PGs* in Fig. 9. Its size relative to the size of the *P* wave (Fig. 9) varies greatly as a function of the sedimentary model. The same large variation in the amplitude ratio can be seen in the observed data (Figs. 6 and 7). Within these wide limits there is agreement between the observed and computed data.

Traces 2, 3 and 4 have a sedimentary layer with a velocity of 3.0 km/s and increasing thickness from 0.5, 1.0 to 2.0 km. The conversion at the bottom of the sediments alters the signal very strongly. The reverberations within the sedimentary layer extend over the entire time interval to the Moho conversion *PMs*, which comes 4 s after *P* (see trace 4 especially). This means that realistic sedimentary layers underneath the GRF stations may interfere with possible conversion from the central or lower crust, which makes it very difficult to distinguish between such conversions and multiples within the sediments. The observed data in Figs. 1 and 2 seem to have more correlatable phases between *PGs* and *PMs*. But it is very likely that these phases are multiples in the sediments and not conversions from the middle crust.

Traces 5 and 6 are for models with high-velocity (5 km/s) Jurassic sediments at the surface (see Table 3), but these sediments have only very little influence on the converted waves (compare traces 4 and 5 and traces 2 and 6). Traces 7 and 8 belong to models which have linear gradients in the sediments instead of homogeneous layers. Such models preserve the incoming waveforms and generate only small multiples.

Traces 9, 10 and 11 model approximately the sedimentary layers under stations A1, B1 and C1 (Geologische Karte von Bayern, München, 1981). Although the models used to compute traces 9, 10 and 11 are very similar to those used to compute traces 4, 3 and 2, these traces themselves differ considerably. This means that small modifications of realistic sedimentary models under the GRF stations can have significant influences on the entire wave train between the first onset and the Moho conversion *PMs*. It should be noted that the *P* waves in Fig. 9 are also significantly

influenced by the sediments. The simple incoming signal is complicated by the reverberations within the sediments.

## Results and conclusions

Refraction profiles near the GRF array have been interpreted by Aichele (1976). Reflections from the Moho have been observed but no details about the sharpness of the Moho have been obtained. We have observed, in the rotated short-period $Q$ components of the GRF records, clear evidence for the existence of $P$-to-$S$ converted phases at the crust-mantle boundary and at the bottom of the sediments. We have also computed theoretical seismograms of such converted phases for various models of the Moho transition zone and for models of the sediments. The clearest and most important observational result in the data is that the Moho conversion *PMs* differs significantly among the stations A1, B1 and C1. It is strongest at B1 (where it has about the same size as the conversion *PGs* at the bottom of the sediments); it is smaller at A1 (where it is about half the size of *PGs*); and it is not observable at C1 (see Figs. 1–3). But *PGs*, in contrast, is strongest at C1, weaker at A1 and weakest at B1 (see Figs. 6 and 7).

Theoretical seismograms of converted waves for different models of the sediments (Fig. 9) show that the *PGs* wave group may influence the entire time window to *PMs*. Even *PMs* may be influenced by *PGs* and multiples in the sediments. Therefore, it is difficult to identify additional conversions from other parts of the crust (this could be different for stations on different geological structures). For this reason it is also difficult to obtain a reliable estimate of the absolute amplitude of *PMs* (see Figs. 6 and 7). The Moho conversion *PMs* is least influenced by *PGs* at station B1 because *PGs* is relatively small there. Any interpretation of the size of *PMs* must relate this phase to another phase. As we have seen, *PGs* is not very useful for this purpose since it is very unstable across the array. The *P* wave is more useful since it is more stable than *PGs*, but it is also influenced by the sediments (see Fig. 9). Therefore, we try to discuss the amplitudes of *PMs* in relation to both *PGs* and *P*.

At station A1 the ratio of the observed *P* wave to the energy arriving at the time of *PMs* is roughly in agreement with the theoretical ratio in Fig. 7. In this figure the Moho was assumed to be a first-order discontinuity and the sedimentary model has been varied. In all considered cases, *PGs* is clearly larger than *PMs*. This is also in good agreement with the observations at station A1. For these reasons it seems that a first-order discontinuity and almost any sedimentary model can explain the observed data at station A1. Another observation at station A1, but not at B1 and C1, is that the nuclear explosions in Fig. 1 (traces 1–7) have a strong onset at about 15 s after *P*. This could be a multiple within the crust, similar to that produced by the laminated models belonging to traces 6–9 in Fig. 8. This could be an indication that such a lamination would also be a possibility for station A1.

At station B1 *PMs* is clearly stronger in relation to *P* and *PGs* than at A1. Such strong Moho conversions have only been obtained from models with thin low-velocity layers just above the Moho (see traces 12 and 13 in Fig. 8). We are not suggesting a velocity of 5 km/s in the lower crust, we have merely discussed the possibilities we have with laterally homogeneous models.

At station C1 we have observed practically no converted energy at the Moho. A comparison with the theoretical seismograms in Fig. 8 (trace 6) could lead to a model with a thin layer of high-velocity material just above the Moho. Such a model would be sufficient to supress the converted energy. However, trace 6 in Fig. 8 has very strong multiples starting about 12 s after *P*, and there is no indication of that in the data. Trace 5 in Fig. 8 (belonging to a thick transition zone) also reduces *PMs* and does not generate such strong multiples. Therefore, a very thick transition zone seems to be the best model for the Moho underneath C1.

The conclusion from this comparison between observed and computed data is that the crust-mantle transition zone varies significantly across the array. At the northern part of the array a first-order discontinuity with normal velocity contrast or a lamination would explain the data; at the central part we need a transition zone with an increased velocity contrast; and in the southernmost part we need a reduced sharpness of the transition zone. A more quantitative analysis is not intended at this time, but this should be possible with a larger amount of data.

The second important conclusion is that the sediments have a strong influence on the entire wave train between the first onset and the Moho conversion about 4 s later. Correlatable phases certainly exist with time delays smaller than 4 s, but it is not possible to determine if these phases are multiples within the sediments or conversions from deeper parts of the crust.

Another conclusion from the theoretical *P*-wave seismograms in Fig. 9 is that sedimentary layers underneath a station can lead to severe disturbances of the signal form and the amplitude of the incoming *P* wave.

*Acknowledgements.* This research was supported by the Max-Planck-Gesellschaft and the Deutsche Forschungsgemeinschaft. We wish to thank S. Faber for contributing to the discussion, Frank Krüger for providing Fig. 4 and discussions, and Axel Plesinger for the data from KSP and KHC. We also thank M. Hellweg for help in our computations. The first author would also like to thank all his colleagues from the Seismologisches Zentralobservatorium for their help during his visit. We thank Peter Basham and Max Wyss for reading the manuscript.

## References

Aichele, H.: Interpretation refraktionsseismischer Messungen im Gebiet des Fränkisch-Schwäbischen Jura. Dissertation, Universität Stuttgart, 1976

Aki, K., Christofferson, A., Husebye, E.S.: Three dimensional seismic structure of the lithosphere under Montana LASA. Bull. Seismol. Soc. Am. **66**, 501–524, 1976

Bath, M., Stefansson, R.: S-P conversions at the base of the crust. Ann. Geofis. **19**, 119–130, 1966

Bock, G., Ha, J.: Short-period S to P conversion in the mantle at a depth near 700 km. Geophys. J. R. Astron. Soc **77**, 593–615, 1984

Burdick, L.J., Langston, C.A.: Modeling crustal structure through the use of converted phases in teleseismic body waves. Bull. Seismol. Soc. Am. **67**, 677–691, 1977

Faber, S., Müller, G.: Sp phases from the transition zone between the upper and lower mantle. Bull. Seismol. Soc. Am. **70**, 487–508, 1980

Faber, S., Müller, G.: Converted phases from the mantle transition zone observed at European stations. J. Geophys. **54**, 183–194, 1984

Faber, S., Plomerova, J., Babuska, V.: Deep seated lateral velocity

variations beneath the GRF array inferred from mislocation patterns and P residuals. J. Geophys. 1986 (in press)
Harjes, H.-P., Seidl, D.: Digital recordings and analysis of broadband seismic data at the Gräfenberg (GRF) array. J. Geophys. **44**, 511–523, 1978
Kind, R.: The reflectivity method for different source and receiver structures and comparison with GRF data. J. Geophys. **58**, 146–152, 1985
Langston, C.A.: Structure under Mount Rainier, Washington, inferred from teleseismic body waves. J. Geophys. Res. **84**, 4749–4762, 1979
Liu Qiyuan, Fan Hueiji: Matrix-ray method for synthetic seismograms of body waves of earthquakes. Acta Geophysica Sinica 1986 (in press), (in Chinese with English abstract)
Liu Qiyuan, Shao Xuezhong: A study of the dynamic characteristics of PS converted waves with synthetic seismograms. Acta Geophysica Sinica **28**, 291–302, 1985, (in Chinese with English abstract)
Plesinger, A., Hellweg, M., Seidl, D.: Interactive high-resolution polarisation analysis of broadband seismograms. J. Geophys. **59**, 129–139, 1986
Polshkov, M.K., Bulin, K.N., Sherbakova, B.E.: Crustal investigation of the U.S.S.R. by means of earthquake-generated converted waves. Tectonophysics **20**, 57–66, 1973
Shao Xuezhong, Zhang Jiru, Yang Xiaofeng, Zhang Xiaohu, Lei Shengli, Wang Qiming, Gao Weian: An experimental study of the structure of the Earth's crust and upper mantle by converted waves. Acta Geophysica Sinica **21**, 89–100, 1978, (in Chinese with English abstract)
Shao Xuezhong, Zhang Jiaru, Liu Qiyuan, Zhang Siya: The commong features of deep structures in some large earthquake areas of North China plain and their meaning to the earthquake site prediction. J. Phys. Earth 1986 (in press)
Vinnik, L.P.: Detection of waves converted from P to SV in the mantle. Phys. Earth Planet. Inter. **15**, 39–45, 1977
Vinnik, L.P., Avetisjan, R.A., Mikhailova, N.G.: Heterogeneities in the mantle transition zone from observations of P-to-SV converted waves. Phys. Earth Planet. Inter. **33**, 149–163, 1983

Received April 22, 1986; revised version September 23, 1986
Accepted September 29, 1986